X-ray reflected spectra from accretion disk models. I. Constant density atmospheres

J. García

The Catholic University of America, IACS, Physics Department, Washington DC 20064;

and NASA Goddard Space Flight Center, Greenbelt, MD 20771

javier@milkyway.gsfc.nasa.gov

T.R. Kallman

NASA Goddard Space Flight Center, Greenbelt, MD 20771

timothy.r.kallman@nasa.gov

Received _____; accepted _____

ABSTRACT

We present new models for illuminated accretion disks, their structure and reprocessed emission. We consider the effects of incident X-rays on the surface of an accretion disk by solving simultaneously the equations of radiative transfer, energy balance and ionization equilibrium over a large range of column densities. We assume plane-parallel geometry and azimuthal symmetry, such that each calculation corresponds to a ring at a given distance from the central object. Our models include recent and complete atomic data for K-shell of the iron and oxygen isonuclear sequences. We examine the effect on the spectrum of fluorescent Kα line emission and absorption in the emitted spectrum. We also explore the dependence of the spectrum on the strength of the incident X-rays and other input parameters, and discuss the importance of Comptonization on the emitted spectrum.

1. Introduction

The X-ray spectra from active galactic nuclei (AGN) and X-ray binaries often show evidence of interaction between radiation emitted near the compact object and the nearby gas, which leads to signatures imprinted on the observed spectrum. The effects of this reflection include iron K line emission, in the range 6-8 keV, which is observed from nearly all accreting compact sources (Gottwald et al. 1995); and the flattening of the spectrum above 10 keV, usually called high energy bump or the Compton hump, since it originates due to the Compton scattering of photons by cold electrons in the gas.

The profile of the iron K line carries important information about the physics of the material around the compact object. Since the emission may occur in a relatively

small region close to the center, the line profile can be affected by relativistic effects. The best-known example is the Seyfert 1 galaxy MCG-6-30-15 (Tanaka et al. 1995; Iwasawa et al. 1999), for which the iron line appears to be broad and skewed well beyond the instrumental resolution. Model line profiles for Schwarzschild and Kerr metrics have been calculated by Fabian et al. (1989) and Laor (1991), respectively. Brenneman & Reynolds (2006) have used this information to constrain the spin of the black hole harbored by this AGN.

Observations of other accreting systems such as low mass X-ray binaries (LMXB) have also revealed the iron K line in emission. Bhattacharyya & Strohmayer (2007) reported the detection of a broad iron line emission in the *XMM Newton* spectrum of the LMXB system Serpens X-1. Using *Suzaku* observations, Cackett et al. (2008) confirmed this detection and found similar emission in other two LMXBs (4U 1820-30 and GX 349+2). Assuming relativistic broadening and applying the same models used in AGN observations, these authors have derived estimates for the inner radius of the accretion disk which can be used as an upper limit for the radius of the neutron star. Similar behavior appears in the millisecond pulsar SAX J1808.4-3658 (Cackett et al. 2009). Since the temperature of the surface layers of an accretion disk around a stellar-mass black hole or a neutron star is expected to be much higher than the temperature in the accretion disk of an AGN, the Compton down scattering of photons can also modify the emission profile and even contribute to the broadening of the iron K line (Ross & Fabian 2007). Reis et al. (2009) found evidence for such a situation in the *Suzaku* spectrum of the LMXB 4U 1705-44.

An X-ray line propagating in a dense gas has a non-negligible probability of interacting with an electron, which leads to a down scattering of photons. The maximum energy shift per scattering of a photon with energy E_c due to the electron recoil (for backscattered photons at 180°), is $\Delta E_{max} = 2E_c^2/(m_e c^2 + 2E_c)$, where $m_e c^2$ is the electron rest-mass

energy. Many scatterings will therefore produce a discernible "Compton shoulder" between E_c and $E_c - \Delta E_{max}$ (Pozdniakov et al. 1979; Illarionov et al. 1979; Matt et al. 1991). Although the Compton shoulder and the iron Kβ emission line are weaker than the iron Kα emission line, both have been detected in AGN observations, especially those from the X-ray observatory *Suzaku* (Markowitz et al. 2007; Reeves et al. 2007; Yaqoob et al. 2007), and at least in one LMXB, GX 301-2 (Watanabe et al. 2003).

Initial studies of reprocessed radiation by cold matter were due to Lightman & Rybicki (1980) and Lightman et al. (1981), who derived the Green's functions for the scattering of photons by cold electrons and discussed the implications for AGN observations (Lightman & White 1988). George & Fabian (1991) included line production in their Monte Carlo calculations, while photoionization equilibrium was included by Zycki et al. (1994). Several authors expanded these studies assuming constant density along the vertical direction of the disk (Done et al. 1992; Ross & Fabian 1993; Matt et al. 1993; Czerny & Zycki 1994; Krolik et al. 1994; Magdziarz & Zdziarski 1995; Ross et al. 1996; Matt et al. 1996; Poutanen et al. 1996; Blackman 1999), while hydrostatic calculations have been carried out by Rozanska & Czerny (1996); Nayakshin et al. (2000); Nayakshin & Kallman (2001); Ballantyne et al. (2001); Dumont et al. (2002) and Ross & Fabian (2007).

Nevertheless, one of the most significant limitations inherent in current reflection models is the limited treatment of the physics governing the atomic processes affecting the excitation and emission from the ions in the atmosphere, especially the iron K-shell structure. In most cases, reflection models implement analytic fits to the partial Hartree-Dirac-Slater photoionization cross sections of Verner & Yakovlev (1995), together with the line energies, fluorescence and Auger yields from Kaastra & Mewe (1993), which have been proven to be over simplified and incomplete (Gorczyca & McLaughlin 2005). In some cases, the models lack atomic data for any of the neutral species (except for H and He).

In this paper, we present new models for illuminated accretion disks and their structure implementing state-of-the-art atomic data for the isonuclear sequences of iron (Kallman et al. 2004), and oxygen (García et al. 2005). In addition, the energy, spatial and angular resolution of our calculations are greater than previous works. The ionization balance calculations are performed in detail using the latest version of the photoionization code XSTAR. The radiation transfer equation is solved at each depth, energy and angle using the Feautrier formalism. We assume plane-parallel geometry and azimuthal symmetry. For simplicity in this paper we assume constant density along the vertical direction of the atmosphere, and we leave the hydrostatic calculation for future publication.

This paper is organized in the following way. In § 2 we describe the theory and numerical methods used to solve radiation transfer, ionization and energy equilibrium, and the atomic data. In § 3 we present a set of models for constant density atmospheres at different degrees of ionization, viewing and incidence angles, as well as the effect of the abundance on the reflected spectrum. Finally, the main conclusions are summarized in § 4.

2. Methodology

In this section we describe the theory used in our calculations, in particular, the numerical methods to solve the radiation transfer equation, the ionization equilibrium, energy conservation and the new atomic data incorporated in our models.

2.1. Radiative Transfer

The standard form of the transfer equation for a one dimensional, plane-parallel atmosphere is given by

$$\mu \frac{\partial I(z,\mu,E)}{\partial z} = \eta(z,) - \chi(z,E) I(z,\mu,E), \tag{1}$$

where μ is the cosine of the angle with respect to the normal, and $\eta(z,E)$ and $\chi(z,E)$ are the total emissivity and opacity, respectively. It is convenient to write this equation in terms of the Thomson optical depth, $d\tau \equiv -\alpha_s dz = -\sigma_T n_e dz$, where σ_T is the Thomson cross section ($= 6.65 \times 10^{-25}$ cm^2), and n_e is the electron number density, such that

$$\omega(\tau,E)\mu \frac{\partial I(\tau,\mu,E)}{\partial \tau} = I(\tau,\mu,E) - \frac{\eta(\tau,E)}{\chi(\tau,E)} \tag{2}$$

where we have defined

$$\omega(\tau,E) \equiv \frac{\alpha_s}{\chi(\tau,E)}. \tag{3}$$

To solve the equation of radiative transfer we use Lambda iteration in the Feautrier formalism, as described in § 6.3 of Mihalas (1978). By restricting μ to the half-range $0 \leq \mu \leq 1$ to express the radiation field in its incoming and outgoing components, and using the symmetric and antisymmetric averages:

$$u(\tau,\mu,E) = \frac{1}{2}[I(\tau,+\mu,E) + I(\tau,-\mu,E)] \tag{4}$$

$$v(\tau,\mu,E) = \frac{1}{2}[I(\tau,+\mu,E) - I(\tau,-\mu,E)], \tag{5}$$

one can rewrite the Equation 2 as a second order differential equation

$$\mu^2\omega^2(E)\frac{\partial^2 u(\mu,E)}{\partial \tau^2} + \mu^2\omega(E)\frac{\partial \omega(E)}{\partial \tau}\frac{\partial u(\mu,E)}{\partial \tau} = u(\mu,E) - S(E) \tag{6}$$

where we have omitted the obvious dependence on τ. Notice that the second term on the left hand side of the equation appears since we are using the energy-independent Thomson optical depth as length variable, instead of the total optical depth $d\tau(E) = -\chi(z,E)dz$.

The second term in the right-hand side is the source function, which is defined at each depth and frequency as

$$S(E) = \frac{\eta(E)}{\chi(E)} = \frac{\alpha_s J(E) + j(E)}{\alpha_s + \alpha_a} \tag{7}$$

where

$$J(E) = \int_0^1 u(\mu, E) d\mu, \tag{8}$$

is the mean intensity (first moment of the intensity), and $j(E)$ is the thermal continuum plus line emissivity calculated at each depth. Here α_s and α_a are the scattering and absorption coefficients, respectively: the former is defined by the product of the density times the Thomson cross section, while the latter contains the continuum cross section due bound-bound, bound-free and free-free absorption. Both $j(E)$ and α_a are obtained from the ionization balance at each point using XSTAR.

We also consider the redistribution of the photons due to Compton scattering using a Gaussian kernel convolved with $J(E)$. The Gaussian is centered at

$$E_c = E_0(1 + 4\theta - \epsilon_0), \tag{9}$$

where $\theta = kT/m_e c^2$ is the dimensionless temperature, E_0 is the initial photon energy and $\epsilon_0 \equiv E_0/m_e c^2$. The energy dispersion is given by $\sigma = E_0 \left[2\theta + \frac{2}{5}\epsilon_0^2\right]^{1/2}$.

Therefore the total source function at each depth, as a function of the energy, is given by:

$$S(E) = \omega(E) \int dE' J(E') P(E', E) + \frac{j(E)}{\chi(E)} \tag{10}$$

where the kernel function (normalized to unity), can be written explicitly as

$$P(E_c, E_s) = \frac{1}{\sigma \pi^{1/2}} \exp\left[\frac{-(E_s - E_c)^2}{\sigma^2}\right]. \tag{11}$$

As shown by Ross & Fabian (1993), this treatment describes adequately the down scattering of photons with energies less than ~ 200 keV. This approximation is also discussed by Ross

et al. (1978) and Nayakshin et al. (2000). There is an important limitation while using this treatment: if the bin width of a certain energy E_c is greater than 2 times the dispersion of the Gaussian, then there is a large probability for a photon to scatter into its own energy bin, producing a numerical pile up of photons at those energies. We use a logarithmically spaced energy grid, so the resolving power $\mathcal{R} = E/\Delta E$ is a constant that only depends on the number of grid points. Therefore, the bin width is $\Delta E = E/\mathcal{R}$, and the pile up occurs at a critical energy E_p when $\Delta E = 2\sigma(E_p)$; or

$$E_p = m_e c^2 \left[\frac{5}{4\mathcal{R}^2} - \frac{5kT}{m_e c^2} \right]^{1/2}. \tag{12}$$

From the last equation it is clear that the pile up appears only at low temperatures, specifically for temperatures less than $T_p = m_e c^2/4k\mathcal{R}^2$. The lowest resolving power used in this paper is $\mathcal{R} = 350$, and then $T_p \sim 10^4$ °K. We will show later that we consider no cases for which the gas temperature becomes lower than this value. In fact, in the extreme limit of $T = 0$ (and using the same resolving power), the highest pile up energy would be $E_p \sim 1.6$ keV, leaving the high energy part of the spectrum unaffected.

To complete this solution, two boundary conditions are imposed; one at the top ($\tau = 0$), and one at the maximum depth ($\tau = \tau_{max}$). At the top, the incoming radiation field $I(0, -\mu, E)$ is equal to a power law, with photon index and normalization as free (input) parameters in the calculation. Subtracting Equations (4) and (5)

$$u(0, \mu, E) - v(0, \mu, E) = I_{inc} \tag{13}$$

and it is easy to show that

$$v(\tau, \mu, E) = \omega(\tau, E)\mu \frac{\partial u(\tau, \mu, E)}{\partial \tau} \tag{14}$$

therefore at the surface,

$$\omega(0, E)\mu \left[\frac{\partial u(\tau, \mu, E)}{\partial \tau} \right]_0 - u(0, \mu, E) = -I_{inc}. \tag{15}$$

At the lower boundary we specify the outgoing $I(\tau, +\mu, E)$ radiation field to be equal to a blackbody with the expected temperature for the disk:

$$\omega(\tau_{max}, \mu, E)\mu \left[\frac{\partial u(\tau, \mu, E)}{\partial \tau}\right]_{\tau_{max}} + u(\tau_{max}, \mu, E) = B(T_{disk}) \tag{16}$$

This condition appears since we assume that there is an intrinsic disk radiation due the viscosity of the gas (Shakura & Sunyaev 1973). The disk temperature at the lower boundary is then given by

$$T_{disk} = \left[\frac{3GM\dot{M}}{8\pi\sigma R^3}\right]^{1/4} \tag{17}$$

where G is the Newtonian gravitation constant, σ is Stefan's constant, M is the mass of the central object, $\dot{M}$ the mass accretion rate, and R is the distance from the center. It is clear that the properties of the accretion disk are introduced in the calculation by means of the lower boundary condition. Further, since we assume constant density for the gas along the vertical direction, it is customary to parametrize each model by the ratio of the net flux incident at the surface over the density, using the common definition of the ionization parameter (Tarter et al. 1969):

$$\xi = \frac{4\pi F_{\rm x}}{n_e}. \tag{18}$$

Finally, Equations (6),(10),(15) and (16) are converted to a set of difference equations by discretization of depths, energies and angles. The solution of the system is found by forward elimination and back substitution. A full transfer solution requires the Feautrier solution to be iteratively repeated, in order to self-consistently treat the scattering process. This procedure requires $\sim \tau_{max}^2$ iterations (lambda iterations) for convergence.

2.2. Structure of the gas

Given the solution for the radiation field at each point in the atmosphere, we use the photoionization code XSTAR (Kallman & Bautista 2001) to determine the state of the gas

for a given value of the number density. The state of the gas is defined by its temperature and the level populations of the ions. The relative abundances of the ions of a given element and the level populations are found by solving the ionization equilibrium equations under the assumption of local balance, subject to the constrain of particle number conservation for each element. Schematically, for each level

$$\text{Rate in} = \text{Rate out} \tag{19}$$

The processes include spontaneous decay, photoionization, charge transfer, electron collisions, radiative and dielectronic recombination and charge transfer. Similarly, the temperature of the gas is found by solving the equation of thermal equilibrium, which may be written schematically as

$$\text{Heating} = \text{Cooling} \tag{20}$$

The heating term includes photoionization heating (including the Auger effect), Compton heating, charge transfer and collisional de-excitation. The cooling term includes radiative and dielectronic recombination, bremsstrahlung, collisional ionization, collisional excitation of bound levels and charge transfer. All processes include their respective inverses so that the populations approach to local thermodynamic equilibrium (LTE) values under the appropriate conditions (i.e., high density or Planckian radiation field).

2.3. Radiative equilibrium

XSTAR calculates level populations, temperature, opacity and emissivity of the gas assuming that all the physical processes mentioned in the previous section are in steady state. Radiative equilibrium is achieved by calculating the integral over the net emitted and absorbed energies in the radiation field (E_c and E_h, respectively); and varying the gas

temperature until the integrals satisfy the criterion

$$\frac{E_h - E_c}{E_h + E_c} \leq 10^{-4}. \tag{21}$$

The radiative equilibrium condition must be ensured also while solving the transfer equation. According to equation (2-83b) in Mihalas (1978):

$$4\pi \int_0^\infty \chi(E) \left[J(E) - S(E) \right] dE = 0, \tag{22}$$

i.e., the total energy absorbed by a volume of material must be equal to the total energy emitted (note that, as in § 2.1, we have omitted the explicit dependence on τ in the equations). By using the definitions of the flux and radiation pressure (second and third moments of the radiation field):

$$H(E) = \int_0^1 v(\mu, E) \mu d\mu \tag{23}$$

and

$$K(E) = \int_0^1 u(\mu, E) \mu^2 d\mu, \tag{24}$$

one can rewrite Equation (14) as

$$H(E) = \omega(E) \frac{\partial K(E)}{\partial \tau}. \tag{25}$$

Taking the derivative with respect to τ and multiplying by $\omega(E)$

$$\omega(E) \frac{\partial H(E)}{\partial \tau} = \omega^2(E) \frac{\partial^2 K(E)}{\partial \tau^2} + \omega(E) \frac{\partial \omega(E)}{\partial \tau} \frac{\partial K(E)}{\partial \tau}, \tag{26}$$

and comparing with the transfer Equation (6) integrated over μ,

$$\omega(E) \frac{\partial H(E)}{\partial \tau} = J(E) - S(E). \tag{27}$$

From here it is clear that the radiative equilibrium condition (22) is equivalent to

$$\alpha_s \frac{\partial}{\partial \tau} \int_0^\infty H(E) dE = 0, \tag{28}$$

i.e., the net flux must be conserved for any optical depth. Further, inserting the source function (7) in the right-hand side of (27):

$$\frac{\partial}{\partial \tau} \int_0^\infty H(E) dE = \frac{1}{\alpha_s} \int_0^\infty \left[j(E) - \alpha_a J(E) \right] dE = 0. \tag{29}$$

The conservation of the flux through the atmosphere is formally equivalent to the thermal equilibrium condition (20), but its accuracy will depend on the error associated with the evaluation of the right-hand side of Equation (29). Although we require a small error in the calculation of the emissivities $j(E)$ and opacities α_a by imposing the condition (21), the numerical conservation of the flux is a difficult task due to the fact that small errors accumulate over the large column densities covered in the calculation. It can be seen from Equation (29) that the error required in the calculation of emissivities and opacities must be of the order of α_s^{-1}. Assuming that typical values for the density are $n_e \sim 10^{10} - 10^{16}$ cm^{-3}, then $10^8 \lesssim \alpha_s^{-1} \lesssim 10^{14}$, much greater than the value required in (21). Therefore, we also apply a renormalization of the emissivities calculated by XSTAR before the solution of the transfer equation, such that:

$$j^{new}(E) = j(E) \frac{\int_0^\infty \alpha_a J(E) dE}{\int_0^\infty j(E) dE}, \tag{30}$$

at each depth. By implementing this correction in our models, we have found that the net flux (and therefore the energy) is conserved better than 1% for intermediate to large values of the ionization parameter, but the error can be as large as $\sim 15\%$ for low-ionization calculations.

2.4. Atomic data

The XSTAR atomic database collects recent data from many sources including CHIANTI (Landi & Phillips 2006), ADAS (Summers 2004), NIST (Ralchenko et al. 2008), TOPbase (Cunto et al. 1993) and the IRON project (Hummer et al. 1993). The database is described

in detail by Bautista & Kallman (2001). Additionally, the atomic data associated with the K-shell of the Fe ions incorporated in the current version of XSTAR has been recently calculated and represents the most accurate and complete set available to the present. Energy levels and transition probabilities for first row ions Fe XVIII-Fe XXIII were reported by Palmeri et al. (2003a); for second row ions Fe X-Fe XVII were reported by Mendoza et al. (2004); and for the third row ions Fe II-Fe IX by Palmeri et al. (2003b). The impact of the damping by spectator Auger resonances on the photoionization cross sections was discussed by Palmeri et al. (2002). Photoionization and electron impact cross sections were presented for the first row by Bautista et al. (2004), and photoionization cross sections for second row ions by Bautista et al. (2004). Energy levels, transition probabilities and photoionization cross sections for Fe XXIV were calculated by Bautista et al. (2003). A compilation of these results and a careful study of their impact on the photoionization models can be found in Kallman et al. (2004). Moreover, XSTAR also includes the atomic data relevant to the photoabsorption near the K edge of all oxygen ions calculated by García et al. (2005).

The approach used by these authors for the computation of the atomic parameters of iron and oxygen was based on the implementation and comparison of results obtained from different atomic codes of public domain, namely AUTOSTRUCTURE (Badnell 1997), HFR (Cowan 1981), and the Breit-Pauli R-Matrix package (BPRM, Seaton 1987; Berrington et al. 1987).

2.5. Iteration procedure

Starting at the top of the disk, the vertical structure of the gas is found by solving ionization and thermal balance at each spatial zone using XSTAR, as described in § 2.2. Since the radiation field is unknown the first time this is done, it is set to be equal to the incident power law at each depth. Once the last zone is reached, the temperature and

density profiles are known, as well as the emissivities and opacities for each depth and energy. With this information the radiative transfer Equation (6) is solved as described in § 2.1 until the solution converges, which requires $\sim \tau_{max}^2$ Lambda iterations. This provides a new and more accurate radiation field, that can be used to recalculate the structure of the gas. Because the emissivities and opacities are updated when the structure of the gas is recalculated, the radiative transfer calculations must be also repeated. We then continue with this process until all quantities stop changing within a small fraction. Typically, this requires ~ 20 gas structure calculations, times τ_{max}^2 Lambda iterations.

For our purposes, we desire to cover the largest optical depth possible for realistic computational times and resources. Since Lambda iteration requires τ_{max}^2 loops to converge, we performed different numerical experimentation changing the value of τ_{max}. Comparisons with the semi-analytic solution by Chandrasekhar (1960) showed that the error behaves, in general, as $\sim 1/\tau_{max}$, corresponding to a leakage of energy through a scattering dominated slab. The comparison also showed that diminishing improvement is achieved after $\tau_{max} \sim 10 - 20$, taking into account the required number of iterations. Therefore we limit all our calculations to $\tau_{max} = 10$, with the understanding that our resulting global energy budget may be in error by as much as 10%. Finally, our calculations consider high resolution spectra with an energy grid of at least 5×10^3 points ($\mathcal{R} = E/\Delta E \sim 350$), 200 spatial zones, and 50 angles to account for anisotropy of the radiation field.

3. Results

In this section we show the results obtained with our model for constant density atmospheres. We present a total of 20 reflection models, calculated for various representative conditions. These models and input parameters used to produce them are summarized in Table 1. The first column of the Table contains an identification number assigned to

each model and it will be used for reference through the rest of this paper. The next columns contain the input parameters that have been varied for each model, namely: the ionizing flux $F_{\rm x}$, the resulting logarithm of the ionization parameter ξ (see Equation 18), the spectral energy resolution or resolving power $\mathcal{R} = E/\Delta E$ (determined by the number of energy grid-points used), the cosine of the incidence angle of the illuminating radiation with respect to the normal of the disk μ_0, and the abundance of iron normalized to its solar value $\rm A_{Fe}$. Other input parameters not listed in the Table since they are constant and common to all the models are: density $n_e = 10^{15}$ cm^{-3}, photon index of the incident radiation $\Gamma = 2$, mass of the central object $M = 10^8$ M$_\odot$, distance from the central object $R = 7R_s$, and the mass accretion rate $\dot{M} = 10^{-3}\dot{M}_{Edd}$, where $R_s = 2GM/c^2$ is the Schwarzschild radius and $\dot{M}_{Edd}$ is the accretion rate at the Eddington limit. We have chosen these parameters such that the numbers are similar to those typically used by previous authors. However, note that these parameters only affect the present models by changing the effective temperature of the disk (equivalent to changing the intrinsic disk flux), to be used as the inner boundary condition (16) in the radiation transfer problem. Specifically, by using Equation (17) this set of parameters correspond to an intrinsic disk flux of $F_{disk} = 3.6 \times 10^{13}$ erg/cm^2/s, or an effective temperature of $T_{disk} = 2.8 \times 10^4$ °K, which represents a cold disk when compared to the temperatures typically produced by the illuminating fluxes used in this paper. This is convenient since it allows us to analyze the reprocessed spectrum as a direct consequence of the incident power law without significant modifications due to the black body of the disk.

3.1. Temperature profiles

The Figure 1 shows the temperature profile as a function of the Thomson optical depth resulting from constant density models for ten different ionization parameters

Table 1. List of reflection models with their respective input parameters

Model	F_x[a]	logξ[b]	$\mathcal{R}$	μ_0	A_{Fe}
101	1×10^{15}	1.1	350	0.71	1.0
102	2×10^{15}	1.4	350	0.71	1.0
103	5×10^{15}	1.8	350	0.71	1.0
104	1×10^{16}	2.1	350	0.71	1.0
105	2×10^{16}	2.4	350	0.71	1.0
106	5×10^{16}	2.8	350	0.71	1.0
107	1×10^{17}	3.1	350	0.71	1.0
108	2×10^{17}	3.4	350	0.71	1.0
109	5×10^{17}	3.8	350	0.71	1.0
110	1×10^{18}	4.1	350	0.71	1.0
111	5×10^{15}	1.8	3500	0.71	1.0
112	5×10^{16}	2.8	3500	0.71	1.0
113	5×10^{17}	3.8	3500	0.71	1.0
114	1×10^{17}	3.1	350	0.95	1.0
115	1×10^{17}	3.1	350	0.50	1.0
116	1×10^{17}	3.1	350	0.05	1.0
117	5×10^{16}	2.8	350	0.71	0.2
118	5×10^{16}	2.8	350	0.71	2.0
119	5×10^{16}	2.8	350	0.71	5.0
120	5×10^{16}	2.8	350	0.71	10.0

[a]erg/cm^2/s

[b]erg cm/s (See Equation 18)

(models 101-110 in Table 1). In the Figure, the leftmost curve corresponds to the least ionized case, and each consecutive to a higher value of $F_{\rm x}$. The values of the ionization parameters are included next to the respective curves. Because the τ grid is fixed with logarithmic spacing, the surface of the disk is in practice chosen to be $\tau_{top} = 10^{-2}$. The optical depth is measured from the surface towards the interior of the disk. Since the density is assumed to be constant, all these calculations are carried out along a distance of $\Delta z = \Delta\tau/\sigma_T n_e \sim 1.5 \times 10^{10}$ cm.

These curves show very similar general behavior; the temperature is higher at the surface (due to the heating by the incident radiation) and decreases towards the interior of the disk, reaching a minimum temperature. For the high illumination cases (large values of ξ, and/or very close to the surface), the dominant mechanism is Compton heating and cooling (Krolik et al. 1981), with a rate given by:

$$n_e\Gamma_e = \frac{\sigma_T}{m_e c^2}\left[\int EF(E)dE - 4kT\int F(E)dE\right], \tag{31}$$

in the non relativistic limit. When this process dominates, the temperature approaches an asymptotic value, the *Compton temperature*, given by the balance of the two terms in the previous equation:

$$T_{\rm IC} = \frac{< E >}{4k}, \tag{32}$$

where

$$< E >= \frac{\int F(E)EdE}{\int F(E)dE} = F_{\rm x}^{-1}\int F(E)EdE \tag{33}$$

is the mean photon energy. From Equations (32) and (33) it is clear that $T_{\rm IC}$ only depends on the shape of the spectrum. In particular, for the incident power law used in this paper ($\Gamma = 2$), the Compton temperature of the radiation is $T_{\rm IC} = 2.8 \times 10^7$ °K. Note that the temperature at surface for the case with $\log\xi = 4.1$ (model 110) is indeed very close to $T_{\rm IC}$.

In most cases, the gas remains at the high temperature limit throughout the region where the ionizing radiation field is unchanged from the incident field, thus forming a hot

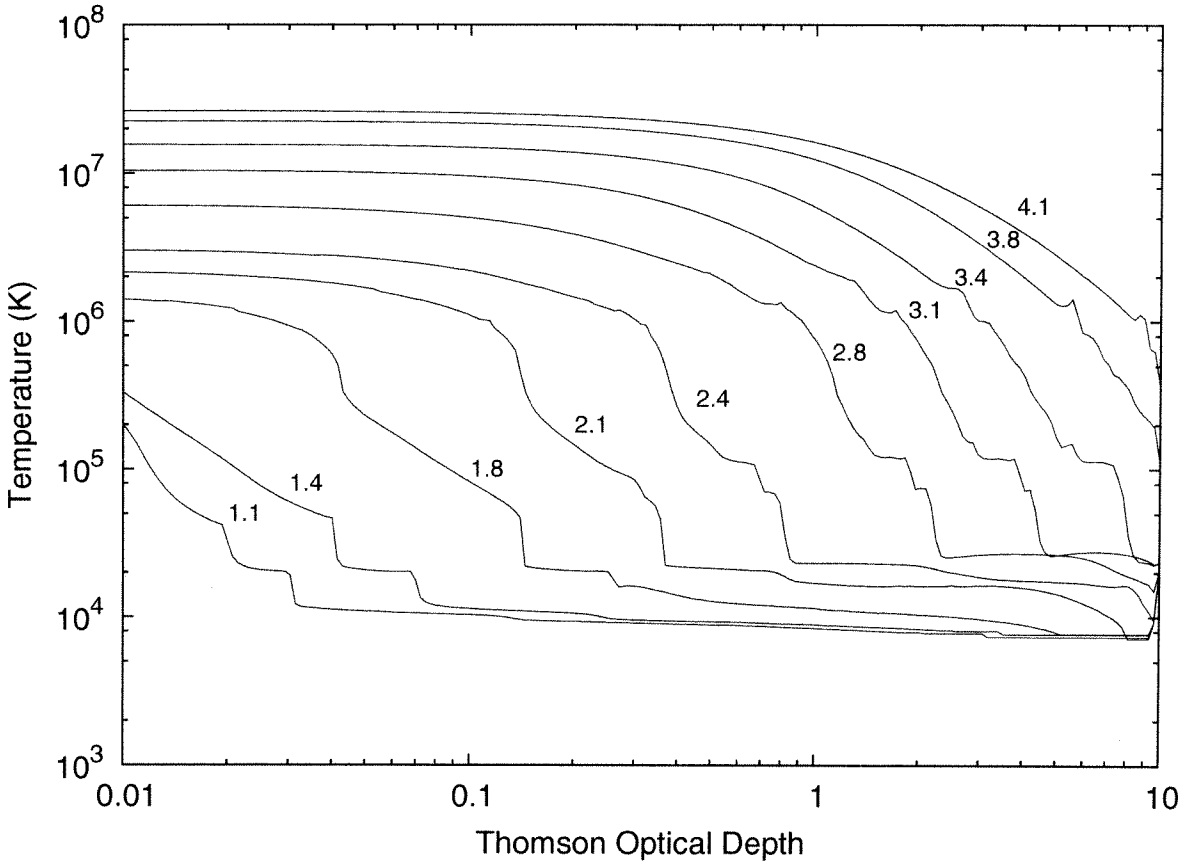

Fig. 1.— Temperature profiles for different illumination fluxes using constant density models ($n = 10^{15}$ cm^{-3}). The value of the ionization parameter ξ is shown next to each corresponding curve (models 101-110).

skin. The temperature gradually decreases in this hot skin as the bremstrahlung cooling becomes more important. As photons are removed from the Lyman continuum energies either by scattering or absorption and re-emission, at some point hydrogen recombines and the opacity grows rapidly, causing a drop in the temperature. Eventually the opacity becomes very large so that few photons are left in the 1-1000 Ry energy range, at which point the radiation field thermalizes to a nearly constant temperature ($T \sim 10^4$ °K).

It is worthwhile to mention that for the models with the two lowest ionization parameters (models 101 and 102), the opacity of the gas is large compared to the ionizing flux even at the surface of the disk and therefore the gas reaches the low temperature limit very rapidly. Conversely, for the two models with $\log\xi = 2.8 - 3.4$ (models 106-108), the illumination is high enough to allow the photons to penetrate much deeper into the atmosphere, and the gas remains at high temperature ($T \sim 10^6$ °K) even for large optical depths ($\tau > 1$). In fact, by looking the intermediate cases (models 103-108), one can clearly identify two temperature zones: the hot skin correspond to $T \gtrsim 10^6$ °K, while the cold region occurs for $T \lesssim 10^5$ °K. Note also that although the transition between the hot and cold regions can be sudden, there is no thermal instability in these calculations, since in all these cases the constant density restriction is applied (Krolik et al. 1981).

3.2. Reflected spectra

Figure 2 shows the reflected spectra for each of the models shown in the previous section (models 101-110 in Table 1). The corresponding ionization parameters are indicated above each curve, starting with the smaller value at the bottom, and increasing the ionization to the top. The curves are shifted to improve clarity. From bottom to top, each consecutive curve is rescaled by a factor increased by one order of magnitude with respect to the previous one (i.e., 1, 10, 100,...,10^9). Strong absorption profiles and edges are

clearly seen in the neutral cases for logξ =1.1, 1.4 and 1.8 (models 101-103), although it is important to mention that some small numerical problems occur in the thermal energy range of the spectrum for the lower flux case. For a few energy bins the reflected outgoing flux becomes negative, due the large opacities for such energies (especially around 100 eV) and numerical errors in calculating the mean intensity. The redistribution of the photons due to Comptonization is evident above 10 keV (Compton bump), and in the smearing of the line profiles. For the models with the lowest illumination (models 101-103), there is a significant modification of the original power law continuum due to the large values of the photoelectric opacity for energies between 100 eV and 10 keV, where most of the strong absorption occurs. Nevertheless, none of these models shows a spectrum dominated by absorption. Even in the lowest ionization case (logξ = 1.1), there are strong emission lines present through the whole energy range. This combination of emission and absorption features in the reflected spectra is a direct consequence of our accurate treatment of radiation transfer and the temperature gradient along the vertical direction of the disk discussed in the previous section.

The iron K line shows the effects of Compton scattering in models with log$\xi \geq 1.8$, since those are the cases for which a hot skin ($T \sim 10^6$ °K) is present for at least a fraction of the total depth of the disk. By comparing the most ionized models, in particular those for logξ = 3.1 and logξ = 3.4 (models 107 and 108), one can see a very drastic change from a highly ionized to an almost featureless spectrum, and even fewer features are seen in the two models for logξ = 3.8 and 4.1 (models 109 and 110). This is due to the fact that in these cases the gas is always at high temperature within the range of our calculations. Despite this, emission from highly ionized iron K lines is still apparent in the reflected spectrum.

Figure 3 shows the same results as Figure 2, but in the 2-10 keV energy range. Here it is possible to see the structure of the iron inner shell transitions in detail. The

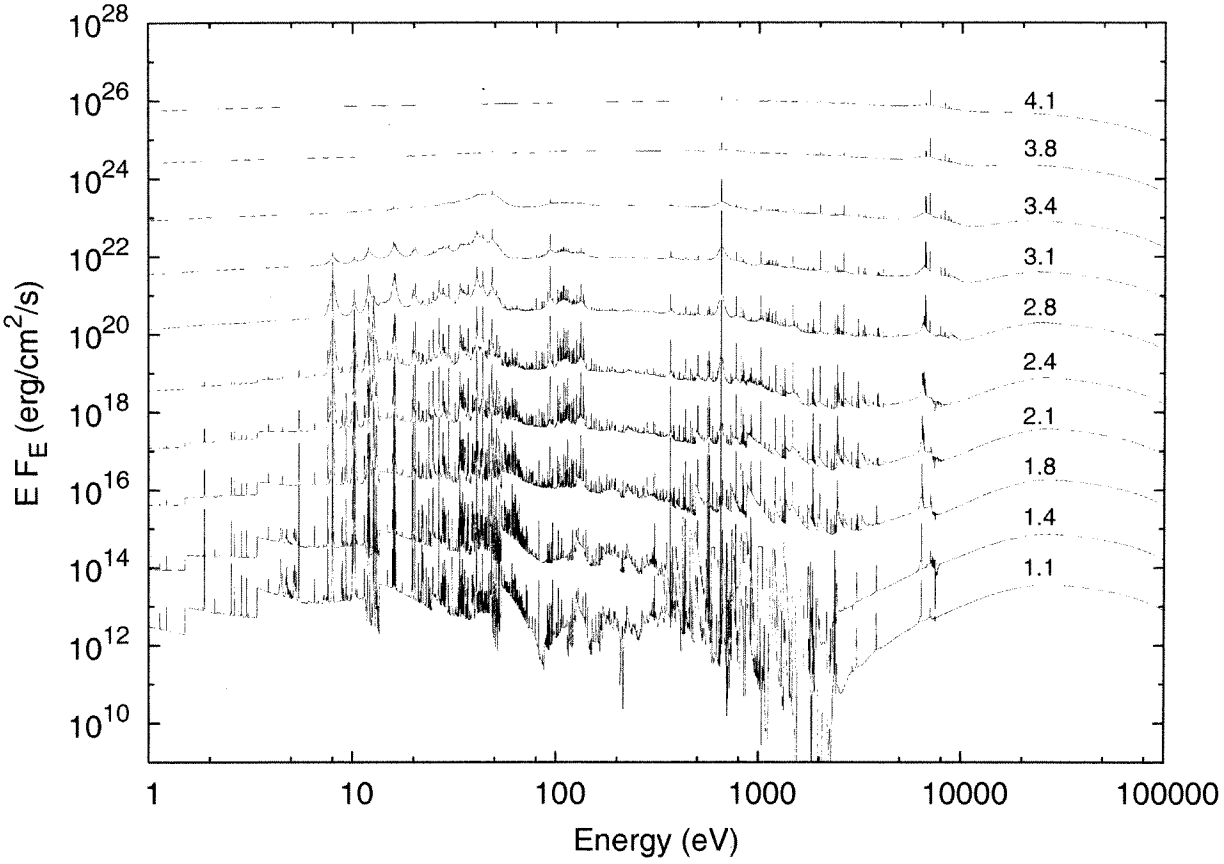

Fig. 2.— Reflected spectra for the models presented in Figure 1. The value of the ionization parameter ξ is shown next to each corresponding curve (models 101-110). The curves are shifted by arbitrary factors for clarity. These are, from bottom to top: 1, 10, 100,...,10^9.

Compton shoulder is apparent in the first three curves from bottom to top (least ionized cases). Changes in the Fe Kα emission line are distinguishable as the ionization parameter increases. The neutral Kβ line is only evident in the three least ionized cases (models 101-103), as well as the Fe absorption edge at $\sim$ 7.5 keV. This figure also shows a more complex structure of the iron line in intermediate cases of ionization: line positions and intensities vary between mostly neutral emission at 6.4 and 7.2 keV for Kα and Kβ, to a very ionized profile with lines around 6.5-7.0 keV and 7.8-8.2 keV for the same transitions.

We have calculated the equivalent widths for the Fe Kα lines in all these spectra. Because of the large deviations of the reprocessed continuum from the incident power law in some of these models (specially for low ξ), in order to calculate the equivalent width we define a local continuum by interpolating a straight line between two points in a the region around the line, specifically between 5.5 and 7 keV. The integration is performed within this range as well, such that only Kα emission is taking into account.

The resulting equivalent widths for the Fe Kα emission line vary between $\sim 400 - 800$ eV for the cases with $1 \lesssim \log\xi \lesssim 3$ (left panel in Figure 3). For higher values of the ionization parameter the equivalent widths decrease very rapidly, to approximately 40 eV for the most ionized case ($\log\xi = 4.1$, model 110). Since the gas is more ionized for high illumination, the emission of the line becomes exclusively due to H- and He-like iron ions, which combined with the extreme Compton scattering of the photons results in the reduction of the equivalent width of the line. This tendency resembles the X-ray Baldwin effect (Iwasawa & Taniguchi 1993), which have been observed in many active galactic nuclei spectra (e.g., Page et al. 2004).

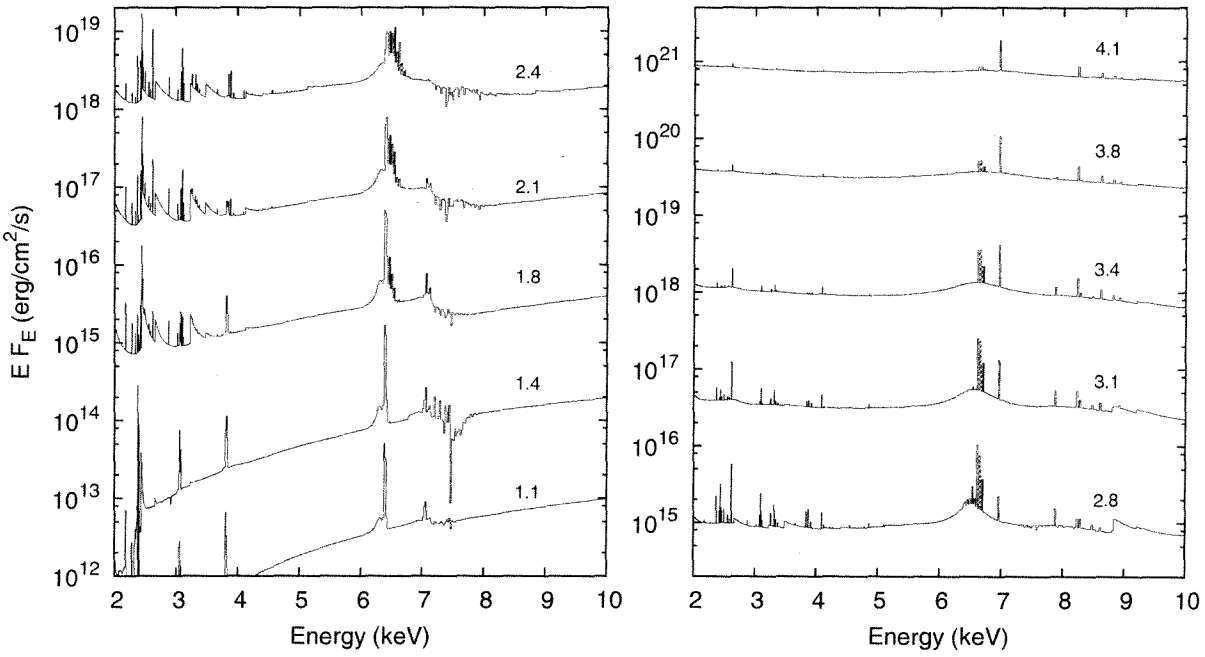

Fig. 3.— Reflected spectra as shown in Figure 2 in the 2-10 keV region. The value of the ionization parameter ξ is shown next to each corresponding curve (models 101-110). The curves are shifted by arbitrary factors for clarity. These are, from bottom to top in each panel: 1, 10, 100, 10^4, 10^5.

3.3. Spectral features

In order to provide a finer analysis of the reflected spectra, we perform calculations increasing the energy resolution by an order of magnitude, i.e., using 5×10^4 energy grid-points ($\mathcal{R} \sim 3500$). Since these calculations are more expensive in terms of CPU-time, we only show three representative cases. These calculations are shown in Figures 4-6, and correspond to models 111, 112 and 113 in Table 1. These spectra (Figures 4-6), are plotted in their physical units and without any renormalization or rescaling, and besides the much higher energy resolution, all the other input parameters in the models are the same as the ones used for the models present previously in Figures 1 and 2.

Figure 4 shows the reflected spectra corresponding to $\log\xi = 1.8$ (model 111), in the 0.5-10 keV energy range, while using a resolving power of $\mathcal{R} \sim 3500$. The most prominent and relevant emission lines are identified in the Figure. In general, the spectrum is dominated by many absorption edges plus radiative recombination continua (RRC). RRCs occurs when a free electron is captured by an ion into an unoccupied orbit; if the electron carries more energy than it needs to be bound to the ion, the excess will be radiated as a photon. Emission K lines from H- and He-like nitrogen, oxygen, neon and magnesium are present in the region around and below 2 keV. At higher energies, there is clear emission from Si XII-XXIV and S XV-XVI. The iron Kα and Kβ components are clearly visible at $\sim$ 6.4 keV and $\sim$ 7.1 keV, respectively, as expected from mostly neutral emission. Many lines are blend together in a small region (about 50 eV for each component), but the emission is mainly due to Fe XIII up to Fe XVI. The Compton shoulder in both components is also evident, as well as a very marked absorption edge at $\sim$ 7.5 keV blended with a complex structure of absorption lines. The energy position of the absorption edge indicates that is likely to be produced by Fe XIII-XIV, according to the energies presented in Kallman et al. (2004) (see in particular their Figure 2).

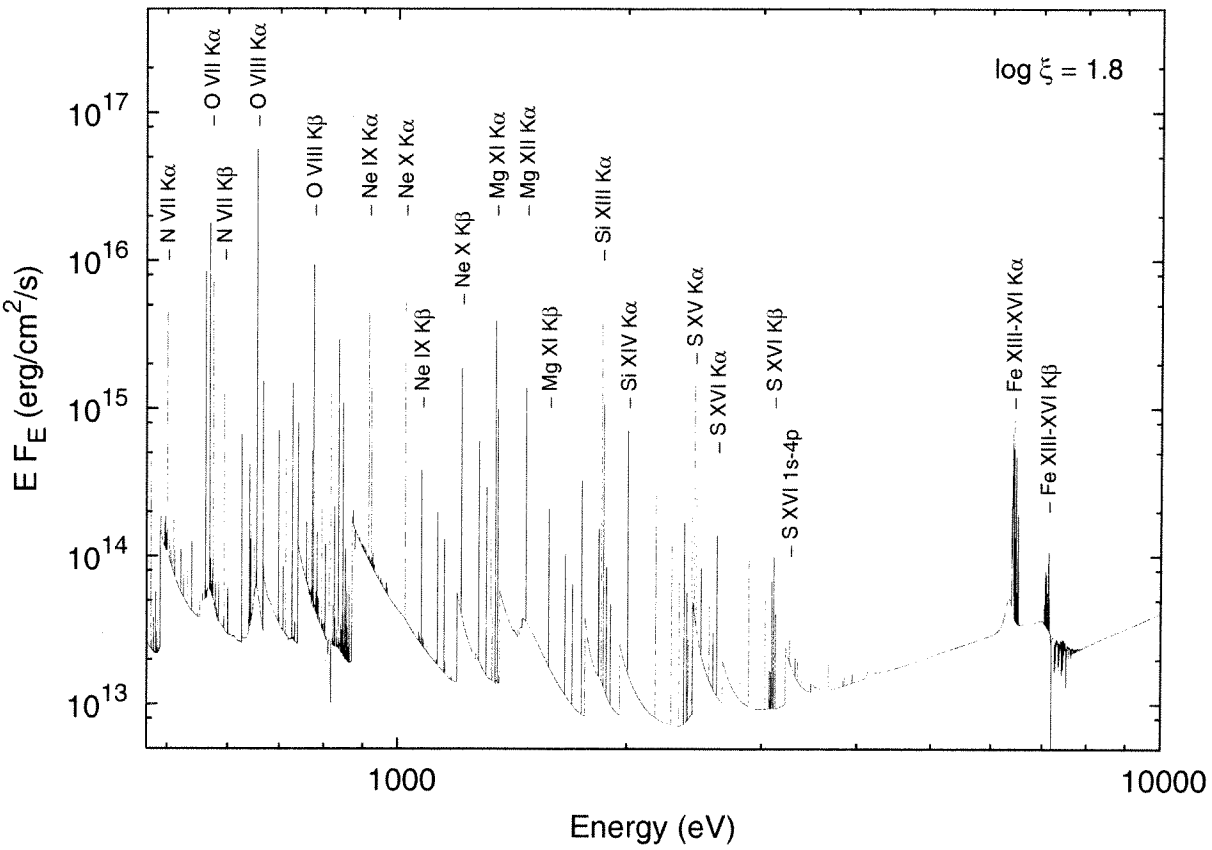

Fig. 4.— Reflected spectra for log$\xi = 1.8$ while using a resolving power of $\mathcal{R} \sim 3500$ (model 111). All the other input parameters are the same used before (as in Figures 1 and 2), although no rescaling is applied. The strongest emission lines are labeled.

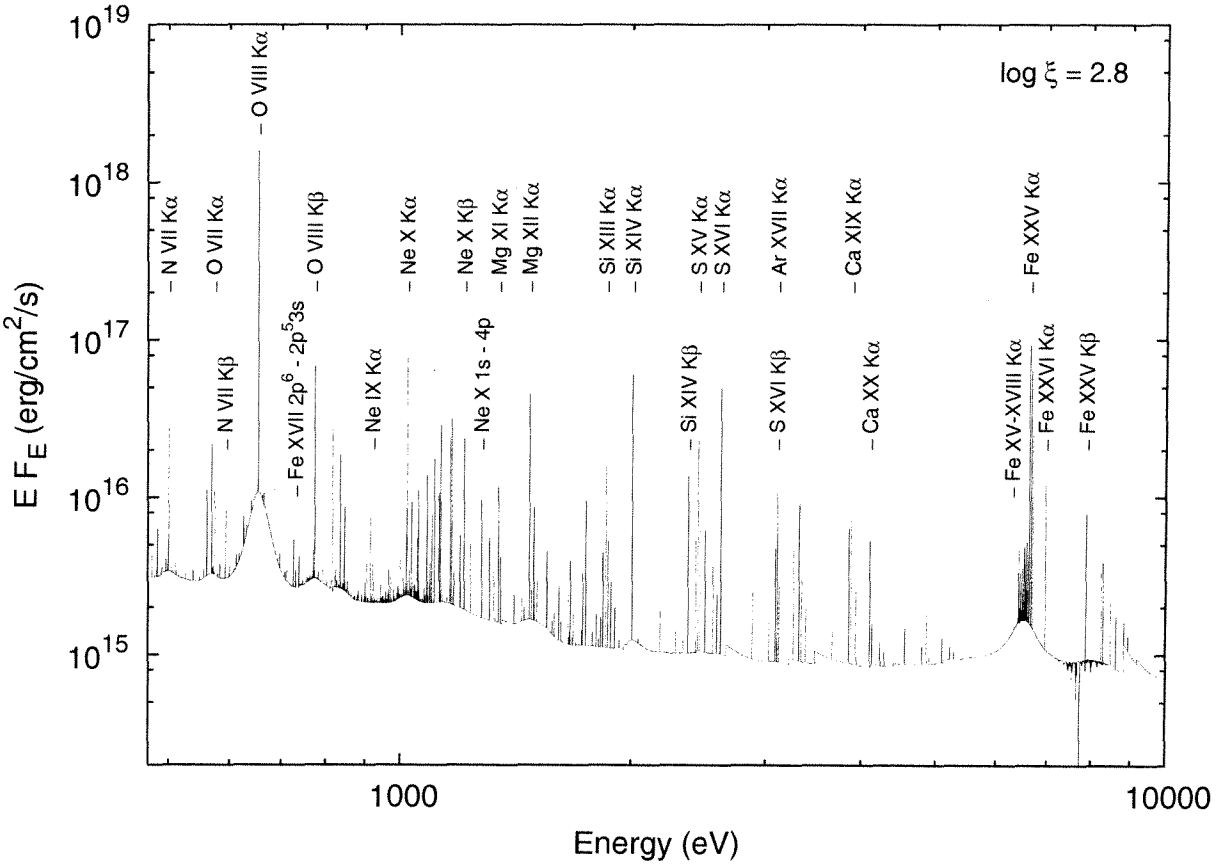

Fig. 5.— Reflected spectra for log$\xi = 2.8$ while using a resolving power of $\mathcal{R} \sim 3500$ (model 112). All the other input parameters are the same used before (as in Figures 1 and 2), although no rescaling is applied. The strongest emission lines are labeled.

Figure 5 shows the resulting spectra when $\log\xi = 2.8$ (model 112), again for a high resolution energy grid ($\mathcal{R} \sim 3500$). There is a significant change in the overall continuum, specially in the 1-10 keV region, in comparison with the previous case ($\log\xi = 1.8$). This is because in the lower ionization case the photoelectric opacity dominates in this energy band and changes the original incident power law shape, while the continuum spectrum in Figure 5 still shows the original slope ($\Gamma = 2$). Lower opacity also allows the efficient propagation of lines (since photons are able to escape), and the emission from heavier elements (Ar XVII, Ca XIX and Ca XX), since the gas is more ionized. In general, this spectrum shows more emission lines and weaker absorption edges. However, some RRCs can still be identified, especially around the sulfur and calcium lines. The K lines from nitrogen, oxygen and neon ions are again the strongest emission features in the low energy part of the spectrum. The high energy region changes noticeably with respect to the previous case with lower ionization. The strongest Fe Kα emission in this case is due to Fe XXV ions at $\sim$ 6.7 keV. However, there is a rich structure of emission lines with centroid energies that cover from $\sim$ 6.4 keV to 6.7 keV produced by ions at lower ionization stages (Fe XV-XVIII). The Fe XXVI Kα emission line is clearly observable at 6.965 keV. All these lines are superimposed on a very broad, Comptonized profile. The Kβ component is replaced by a few distinguishable emission lines mainly due to H- and He-like iron, and a very rich structure of absorption profiles. A small absorption edge can be seen at $\sim$ 9 keV.

It is important to notice that the O XVIII Kα emission line shows the same kind of broadening as the Fe K line. In fact, the other oxygen lines also show broadening in some degree, as well as those coming from neon. This is somewhat unexpected, since photons at those energies would need many scatterings in order to produce such broadening if the gas were cold. However, since the temperature is high ($T \sim 10^6$ °K) even at $\tau \sim 1$, broadening also takes place through the dependence of the Gaussian kernel on the temperature (see § 2.1). This also means that the H-like oxygen lines are being produced efficiently over

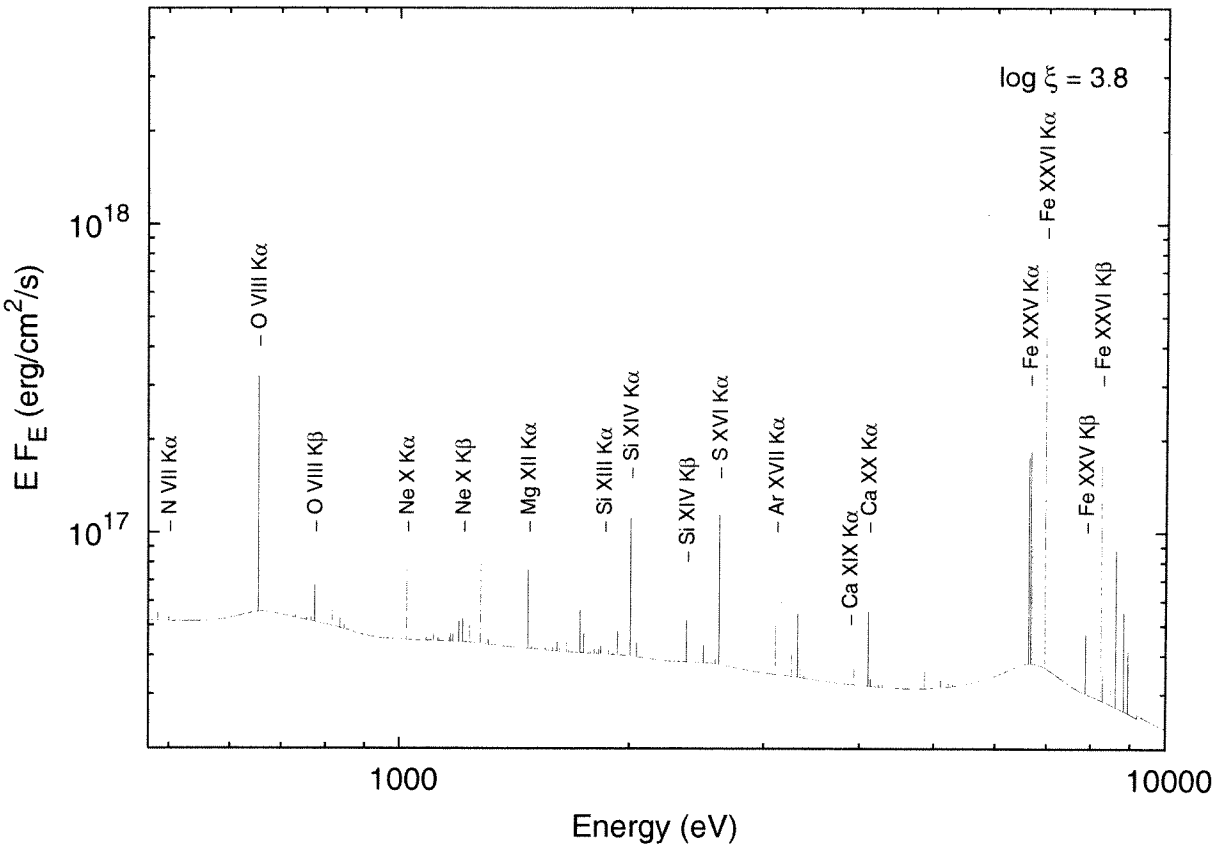

Fig. 6.— Reflected spectra for log$\xi = 3.8$ while using a resolving power of $\mathcal{R} \sim 3500$ (model 113). All the other input parameters are the same used before (as in Figures 1 and 2), although no rescaling is applied. The strongest emission lines are labeled.

a large range of optical depths, which can be verified by looking at higher ionization parameters. Figure 6 shows the last model with a resolving power of $\mathcal{R} \sim 3500$, resulting from a gas at $\log\xi = 3.8$ (model 113). Almost no absorption features can be seen in this spectrum, and the emission consists of mostly fully ionized ions. Both iron and oxygen Kα line profiles are very broad and Comptonized. There are no apparent signs of broad components in the weaker lines, such as those from neon, although this is likely due to the fact that the redistribution is so extreme that it completely smears the profile over the continuum. Therefore, only those photons produced very close to the surface come out of the slab unscattered. The emission in the iron K region is exclusively due to H- and He-like ions. There is strong emission from the Rydberg series of Fe XXV, namely transitions from 1s 4p, 5p and 6p to the ground state $1s^2$, at 8.62, 8.83 and 8.94 keV, respectively.

3.4. Isotropy: incident and viewing angles

The boundary condition expressed in Equation (13) depends, in general, on the angle with respect to the normal on which the radiation is incident. Isotropic illumination implies that the source of radiation is extended and very close to the region where the calculation takes place. On the other hand, locating the source of the external X-rays at a specific location far away of the accretion disk constrains the angle at which radiation will penetrate in the atmosphere. To account for such a situation, the right hand side of Equation (13) can be expressed as

$$I_{inc} = I_0 \delta(\mu - \mu_0), \tag{34}$$

where μ_0 is the incidence angle. The lower panel of Figure 7 shows the reflected spectra for a constant density model in which $\log\xi = 3.1$ for three different incidence angles (models 114-116 in Table 1). The red curve corresponds to $\mu_0 = 0.95$ (normal incidence), the green curve correspond to $\mu_0 = 0.5$, and the blue curve to $\mu_0 = 0.05$ (grazing incidence). The

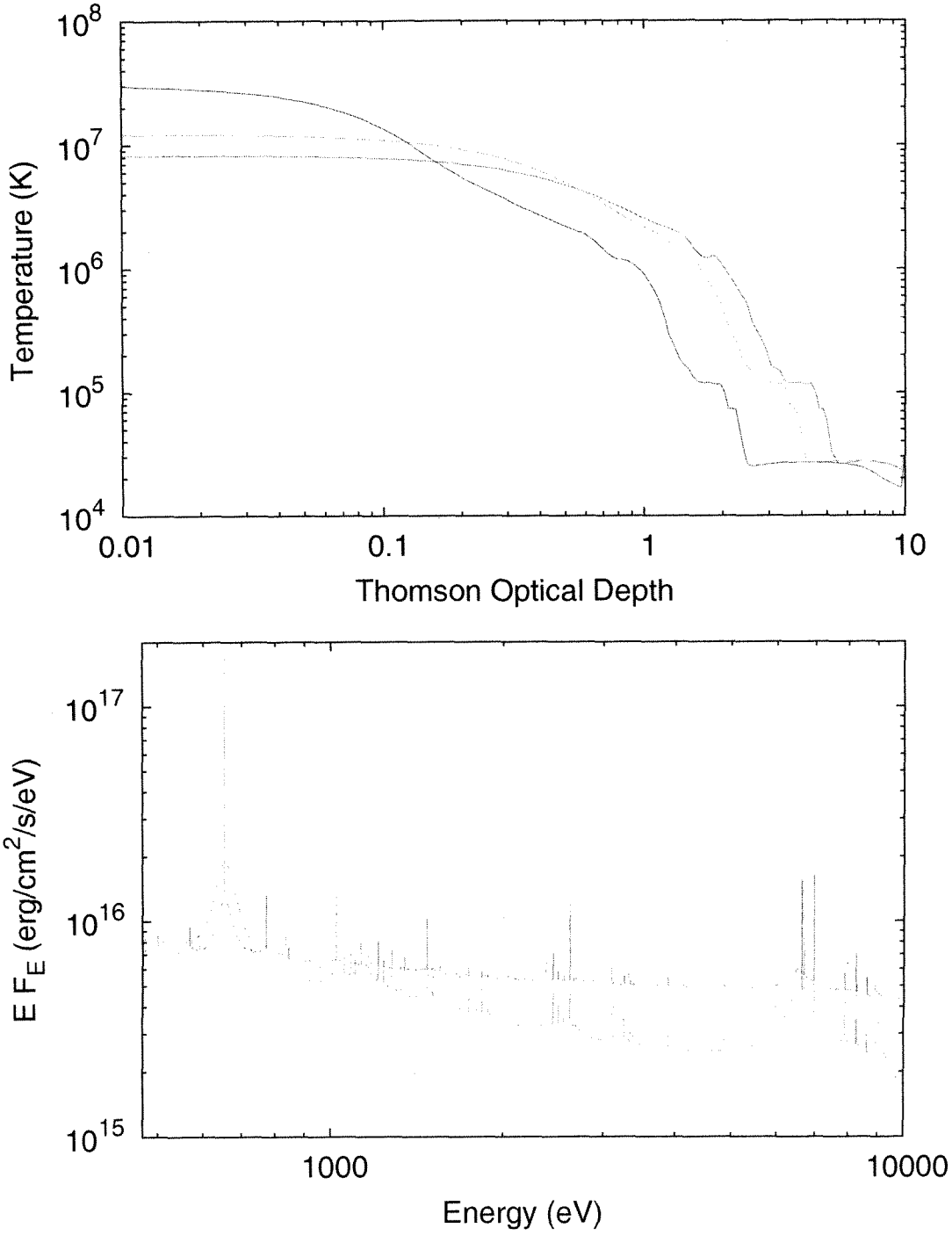

Fig. 7.— Temperature profiles (upper panel) and reflected spectra (lower panel), resulting from a constant density model with logξ = 3.1 for three different incidence angles (models 114-116). In the two panels, the *red* curves corresponds to $\mu_0 = 0.95$ ($\theta \approx 0^o$, normal incidence); the *green* curves to $\mu_0 = 0.5$ (or $\theta = 60^o$); and the *blue* to $\mu_0 = 0.05$ ($\theta \approx 90^o$, grazing incidence).

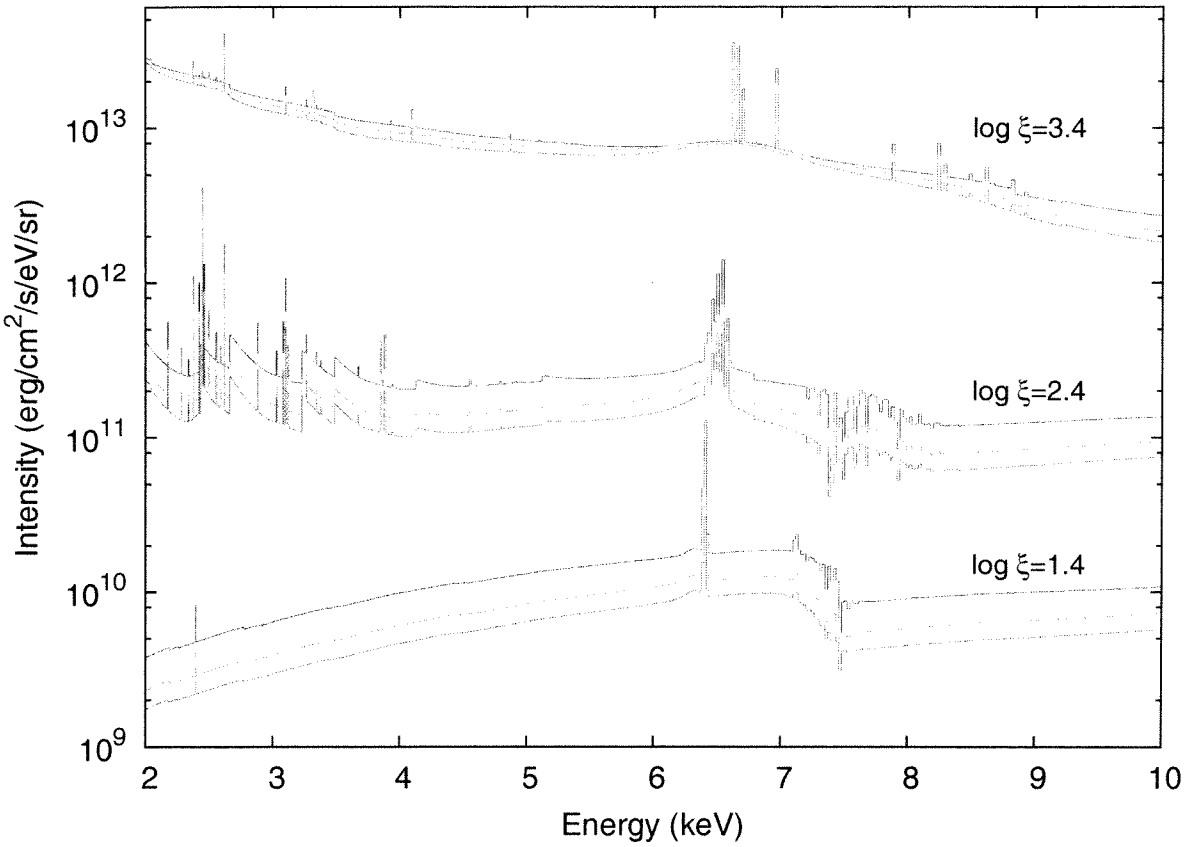

Fig. 8.— Outgoing intensities in the 2-10 keV energy range for constant density models from 3 different ionization parameters (models 102, 105 and 108), as viewed at three different angles with respect to the normal. In all cases, the red curves corresponds to $\mu = 0.95$, the green curves to $\mu = 0.5$, and the blue curves to $\mu = 0.05$.

upper panel of the Figure shows the corresponding temperature profiles as a function of the Thomson optical depth, obtained for each case. At the surface of the disk ($\tau = 0$), the temperature increases with the incidence angle, such that the grazing incidence shows the highest temperature of the three cases. However, when the illumination occurs at normal angles, the radiation ionizes deeper regions in the slab and there is a larger amount of hot material for those cases. In this model, the physical quantity that describes the amount of illumination is the net X-ray flux $F_{\rm x}$, in units of energy per unit area per unit of time. Since the flux is defined as the second moment of the intensity, (Equation 23), therefore $F_{\rm x} = \frac{1}{2}\int I_{inc}\mu d\mu$, and using Equation (34)

$$I_{inc} = \frac{2F_{\rm x}}{\mu_0}\delta(\mu - \mu_0), \tag{35}$$

which means that for the same value of $F_{\rm x}$ (or the same ionization parameter ξ), varying the incidence angle μ_0 effectively varies the intensity of the radiation incident at the surface. This will, of course, produce more heating and raise the temperature and ionization of the top layers in the disk. However, the angular dependence of the radiation field ensures that in the cases of normal incidence the illuminating radiation reaches deeper regions in the atmosphere than those of grazing angles, as is expected. Although the effects on the reflected spectra are not obvious, the spectrum for the grazing incidence (blue curve) is stronger than the other two, mimicking a case of a higher illumination (note that none of the curves have been offset). Nevertheless, the emission lines are, in general, very similar in all cases. It is also interesting to see how the temperature profiles of the three models converge at large optical depths, since the radiation fields become more isotropic after many scatterings.

The isotropy of the reflected radiation field can also be investigated by looking its angular distribution through different viewing angles. Figure 8 contains the reflected spectra for 3 different ionization parameters (indicated next to each case), as is observed from 3

different angles with respect to the normal, in the 2-10 keV energy range. For consistency the colors represent the same angles as in Figure 7, i.e., the red curves indicate $\mu = 0.95$ (face-on), the green curves $\mu = 0.5$, while the blue curves correspond to $\mu = 0.05$ (edge-on). Note that no rescaling or normalization is applied to these curves, therefore the differences are exclusively due to the differences in the ionizing fluxes and on the viewing angles. Moreover, the physical quantity plotted here is the outgoing specific intensity $I(0, +\mu, E)$ instead of the flux (as the other Figures), which is an angle averaged quantity. In fact, these 3 cases are those presented in Figures 2 and 3 (models 102, 105 and 108 in Table 1), and thus their temperature profiles correspond to those shown in Figure 1. In general, the reprocessed features are stronger when the disk is observed face-on than when the viewing angle is parallel to the surface. Nayakshin et al. (2000) found the same tendency in their hydrostatic models, which they explained to be a consequence of an effective Thomson depth that changes when the slab is observed at different angles, according to the geometrical projection $\tau_{eff} = \tau/\mu$. However, their results suggest that the reflection features almost disappear for small values of μ, and that no visible iron could been detected in such cases. The results shown in Figure 8 do not completely agree with this, since the Fe K lines are strong even for the high ionization case. Nevertheless, one must take this comparison with care, since all the results presented in this paper correspond to constant density models, while Nayakshin et al. (2000) calculations were done under hydrostatic equilibrium. In any case, the trend in the emerging spectra shown in Figures 7 and 8 is similar to previous models in the literature, such as those by Nayakshin et al. (2000) and Ballantyne et al. (2001).

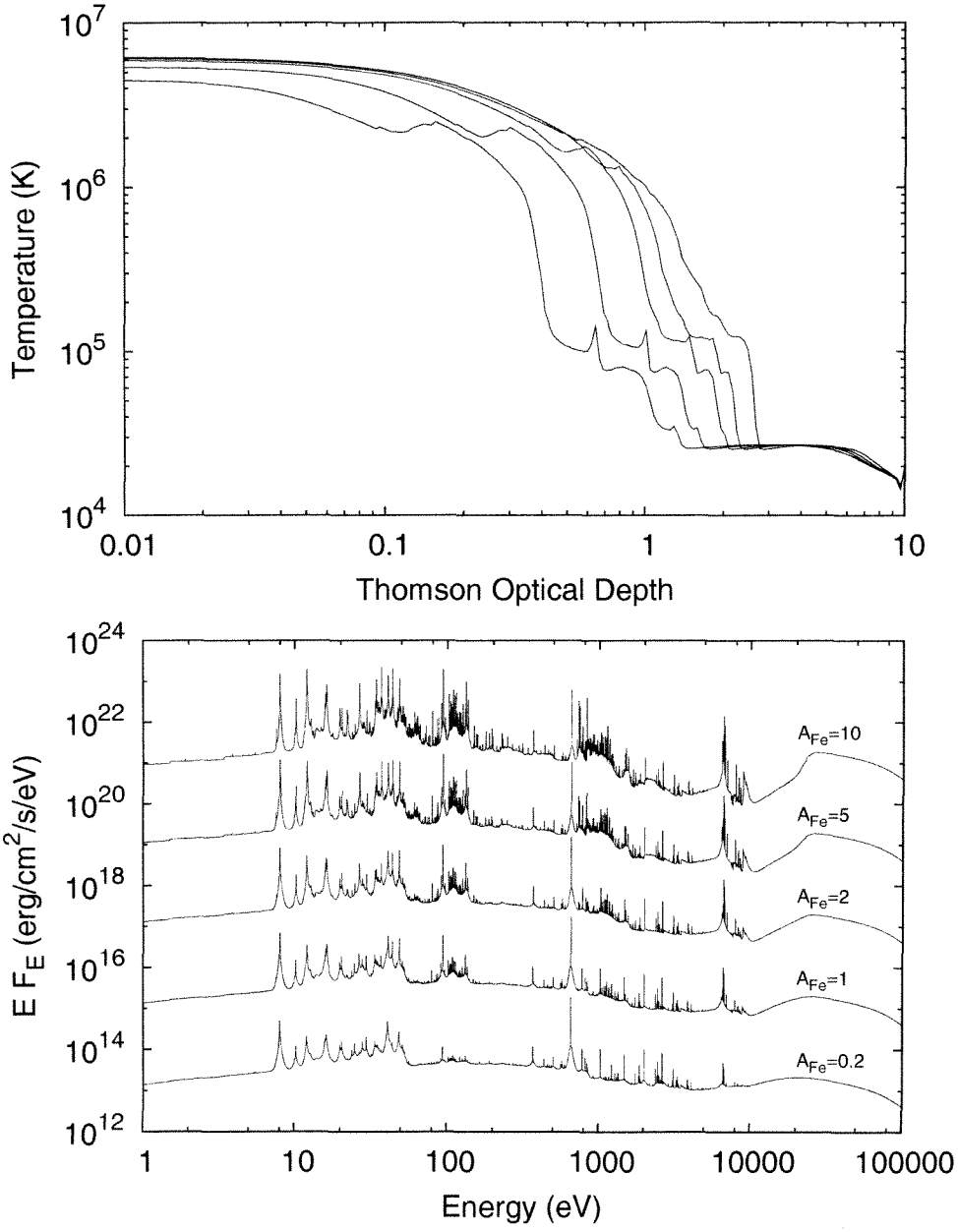

Fig. 9.— *Upper panel*: temperature profiles from a constant density model with $\log\xi = 2.8$ and different iron abundances with respect to the solar values. From left to right, each curve correspond to: A_{Fe}=0.2, 1, 2, 5 and 10 (models 117, 106 and 118-120, respectively). *Lower panel*: reflected spectra for the same models. The curves are shifted by arbitrary factors for clarity. These are, from bottom to top: $10^{-2}, 10^{0}, 10^{2}, 10^{4}$, and 10^{6}. The values of the iron abundance are shown at the top of each curve.

3.5. Iron abundance

We have also studied the effects of the iron abundance on the ionization of the atmosphere and the reprocessed spectra. The upper panel of Figure 9 shows the temperature profiles along the vertical direction for a gas at $\log\xi = 2.8$ when the iron abundance is assumed to be 0.2, 1, 2, 5 and 10 times its solar value (models 117, 106 and 118-120, respectively). The solar atomic abundances used in all our calculations are those from Grevesse et al. (1996), and in particular for iron is 3.16×10^{-5} (with respect to the hydrogen). The curves towards the left of the plot correspond to higher values of the iron abundance, which means that the gas is effectively cooler than the solar and sub-solar cases. This shows that the iron produces a net cooling as its abundance is increased. The transition between the hot and cold regions in the gas occurs at lower optical depths for the super-solar abundance models, decreasing the thickness of the hot skin. However, all the models converge to the same temperature in the cold region of the disk ($T \sim 2.5 \times 10^4$ °K).

The corresponding reflected spectra are shown in the lower panel of Figure 9. These curves are shifted by arbitrary factors for clarity, which are, from bottom to top: $10^{-2}, 10^0, 10^2, 10^4$, and 10^6. The iron emission is enhanced when the abundance is increased, as can be clearly seen at $\sim$ 6 keV, $\sim$ 1 keV and $\sim$ 0.1 keV for the K-, L- and M-shell transitions, respectively. It is also evident that the continuum is highly modified in the 1-40 keV energy region, which is where the larger opacity takes place. However, the Compton hump suffers no significant modifications (i.e., if these spectra are placed on the top of each other, there are no differences in the region above 40 keV).

The suppression of the continuum combined with the enhancement of the K-shell emission lines as the iron abundance is increased shows a significant impact on the line equivalent width. When solar abundance is assumed, we found an equivalent width for the Fe Kα of $\sim$ 700. This value is increased to about 1.1, 2.3 and 3.9 keV when iron is chosen to

be twice, five and ten times more abundant, respectively. Conversely, this value decreases to ~ 203 eV for the model when $A_{Fe} = 0.2$.

3.6. Comparison with previous models

Taking into account that our main contribution to the already existing models of accretion disk is the inclusion of the most complete atomic data available (particularly important for iron), we compare our results for constant density accretion disks models with those included in REFLION (Ross & Fabian 2005). Such a comparison is shown in Figure 10 where the reflected spectra for three different ionization parameters are shown ($\log\xi = 1.8, 2.8$ and 3.8). In the figure, the black curves correspond to our calculations (models 111-113), while the red curves are the models from REFLION with the same input parameters, although the normalizations are chosen arbitrarily. It is clear from this comparison that these two models show important differences. The Fe K line profile around 6.4 keV from our model shows to be much more intense but with similar widths, and the absorption edge at ~ 7.5 keV to be quite strong (specially for the lower ionization). In fact, the equivalent widths of the iron Kα emission line are quite similar in both models for $\log\xi = 1.8$ (~ 750 eV). However, there are larger discrepancies in the higher ionization cases: our models predicts equivalent widths of 695 eV and 92 eV for $\log\xi = 2.8$ and 3.8, respectively; while REFLION models show values of 489 eV and 39 eV for the same cases, respectively. In general, our models predicts stronger Fe Kα emission, a more complex structure for the Fe absorption edge, and the presence of the Fe Kβ emission line at ~ 7.2 keV, not seen in the REFLION models.

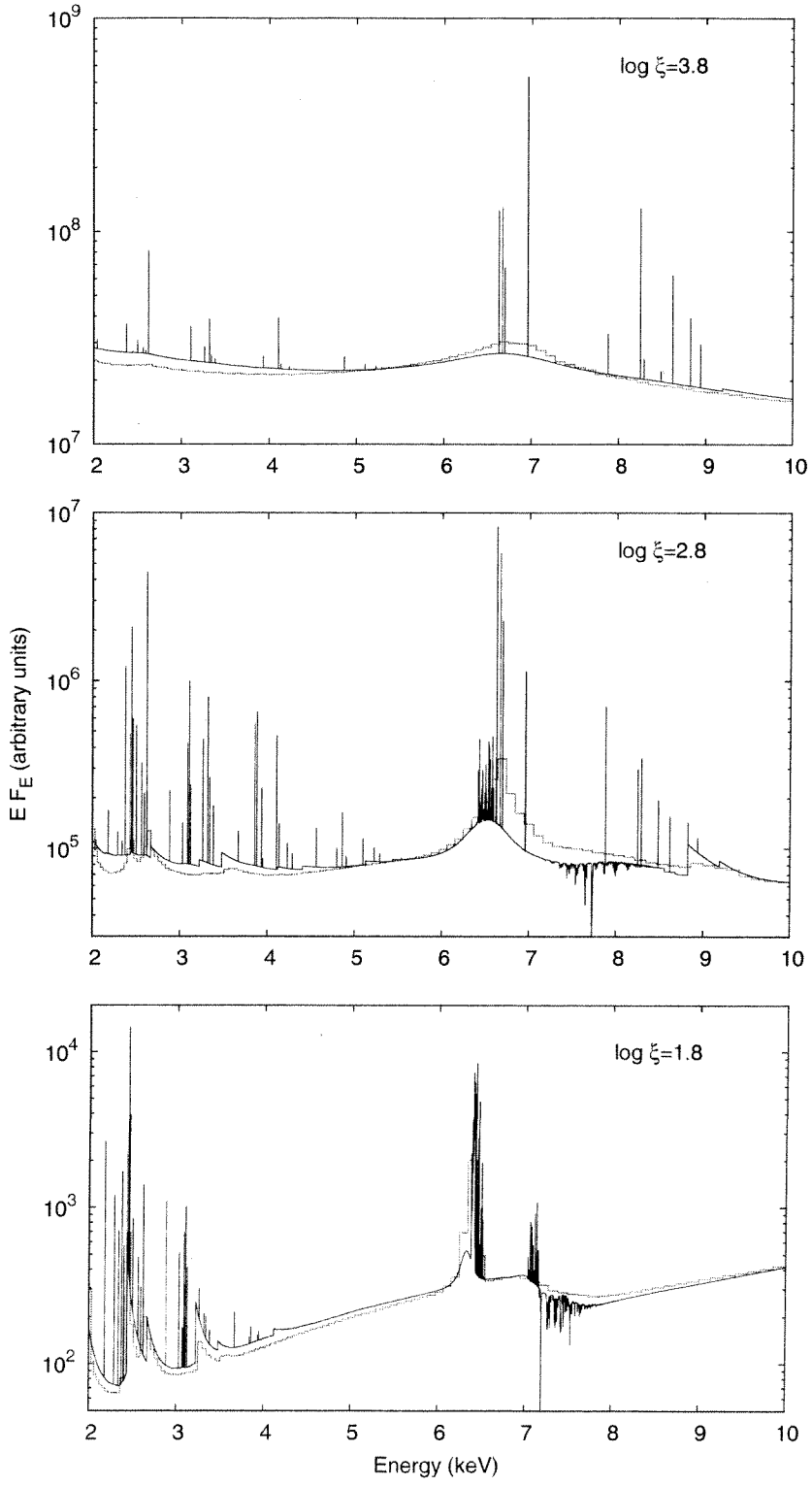

Fig. 10.— Reflected spectra from constant density models for three different ionization parameters (models 111-113), plotted in the 2-10 keV energy range. The red curves are the models from REFLION (Ross & Fabian 2005), for the same input parameters.

4. Conclusions

Answers to outstanding questions concerning accretion disks will not come alone, but with the need to reproduce and predict new observations and to identify spectral profiles at high resolution. In this paper we have presented new models for the structure of X-ray illuminated accretion disks and their reflected spectra, assuming constant density along the vertical direction. These models include the most recent and complete atomic data for the iron isonuclear sequence. The energy resolution used in the reflected spectra exceeds other models previously published as well as the resolution of the detectors on current X-ray observatories (*Chandra, XMM Newton, Suzaku*), and it is comparable to the expected resolving power of the forthcoming International X-Ray Observatory (IXO).

In models with intermediate values of the ionization parameter ($1.8 \leq \log\xi \leq 3.4$), the structure of the gas often displays a two temperature regime: a hot skin ($T > 10^6$ °K) close to the surface where the Compton heating and cooling dominates, and a cold region ($T < 10^5$ °K) where the photoelectric opacity quickly thermalizes the radiation fields. The thickness of the hot skin increases with the illumination, and although these solutions are thermally stable the transition between the hot and cold regions can be sudden. The emerging spectra corresponding to these models show a clear combination of absorption and emission features, specially for $\log\xi < 2.5$. For higher illumination cases the effects of Compton scattering become more evident, even in the low-energy part of the spectrum ($E < 100$ eV). In the high energy part of the spectrum Compton scattering partially smears the profile of the iron K line. The Compton hump above 10 keV is clearly visible in all the models consider here.

The equivalent width of the Fe Kα emission line varies between $\sim$ 400-800 eV for models with $1 \lesssim \log\xi \lesssim 3$. Once the ionization parameter is larger than 10^3, the equivalent width decreases drastically. The lowest value of the equivalent width is $\sim$ 20 eV,

corresponding to the highest illumination case ($\log\xi = 4.1$). This behavior resembles the X-ray Baldwin effect, recently observed in several AGNs. A comparison with other models previously published such as REFLION shown important differences in the structure of the iron K lines. In particular, the equivalent widths in those models can differ by a factor of 2 when compared to the ones shown in this paper.

In general, our simulations show that the K-shell atomic data is crucial to properly model the structure and profile of the iron lines. These results also suggest that the line emission from Fe ions in different ionization stages and Comptonization of high energy photons by cold electrons can be responsible for significant line broadening. These processes need to be taken into account since they can be mistaken for relativistic effects, especially in cases when the gas is partially or high ionized.

Because the state of the gas in the accretion disk depends on the radiation field at each point, and the ionization balance required for a realistic definition of the source function in the radiation transfer depends on both the temperature and density of the gas, a self-consistent approach must be taken into account in order to solve the hydrostatic equilibrium equation instead of assuming constant density. This will be considered as the next step of this project. Future work will also consider the inclusion of new K-shell atomic data recently calculated for the Ne, Mg, Si, S, Ar and Ca by Palmeri et al. (2008a) and Witthoeft et al. (2009), as well as for the nickel isonuclear sequence (Palmeri et al. 2008b).

This work was supported by a grant from the NASA astrophysics theory program 05-ATP05-18. This research has made use of NASA's Astrophysics Data System.

REFERENCES

Badnell, N. R. 1997, J. Phys. B: At. Mol. Opt. Phys., 30, 1

Ballantyne, D. R., Ross, R. R., & Fabian, A. C. 2001, MNRAS, 327, 10

Bautista, M. A., & Kallman, T. R. 2001, ApJS, 134, 139

Bautista, M. A., Mendoza, C., Kallman, T. R., & Palmeri, P. 2003, A&A, 403, 339

—. 2004, A&A, 418, 1171

Berrington, K. A., Burke, P. G., Butler, K., Seaton, M. J., Storey, P. J., Taylor, K. T., & Yan, Y. 1987, J. Phys. B: At. Mol. Opt. Phys., 20, 6379

Bhattacharyya, S., & Strohmayer, T. E. 2007, ApJ, 664, L103

Blackman, E. G. 1999, MNRAS, 306, L25

Brenneman, L. W., & Reynolds, C. S. 2006, ApJ, 652, 1028

Cackett, E. M., Altamirano, D., Patruno, A., Miller, J. M., Reynolds, M., Linares, M., & Wijnands, R. 2009, ApJ, 694, L21

Cackett, E. M., et al. 2008, ApJ, 674, 415

Chandrasekhar, S. 1960, Radiative transfer (New York: Dover)

Cowan, R. D. 1981, The theory of atomic structure and spectra (Berkeley, CA: Univ. of California Press)

Cunto, W., Mendoza, C., Ochsenbein, F., & Zeippen, C. J. 1993, A&A, 275, L5+

Czerny, B., & Zycki, P. T. 1994, ApJ, 431, L5

Done, C., Mulchaey, J. S., Mushotzky, R. F., & Arnaud, K. A. 1992, ApJ, 395, 275

Dumont, A.-M., Czerny, B., Collin, S., & Zycki, P. T. 2002, A&A, 387, 63

Fabian, A. C., Rees, M. J., Stella, L., & White, N. E. 1989, MNRAS, 238, 729

García, J., Mendoza, C., Bautista, M. A., Gorczyca, T. W., Kallman, T. R., & Palmeri, P. 2005, ApJS, 158, 68

George, I. M., & Fabian, A. C. 1991, MNRAS, 249, 352

Gorczyca, T., & McLaughlin, B. 2005, APS Meeting Abstracts, D6037+

Gottwald, M., Parmar, A. N., Reynolds, A. P., White, N. E., Peacock, A., & Taylor, B. G. 1995, A&AS, 109, 9

Grevesse, N., Noels, A., & Sauval, A. J. 1996, in Astronomical Society of the Pacific Conference Series, Vol. 99, Cosmic Abundances, ed. S. S. Holt & G. Sonneborn, 117–+

Hummer, D. G., Berrington, K. A., Eissner, W., Pradhan, A. K., Saraph, H. E., & Tully, J. A. 1993, A&A, 279, 298

Illarionov, A., Kallman, T., McCray, R., & Ross, R. 1979, ApJ, 228, 279

Iwasawa, K., Fabian, A. C., Young, A. J., Inoue, H., & Matsumoto, C. 1999, MNRAS, 306, L19

Iwasawa, K., & Taniguchi, Y. 1993, ApJ, 413, L15

Kaastra, J. S., & Mewe, R. 1993, A&AS, 97, 443

Kallman, T., & Bautista, M. 2001, ApJS, 133, 221

Kallman, T. R., Palmeri, P., Bautista, M. A., Mendoza, C., & Krolik, J. H. 2004, ApJS, 155, 675

Krolik, J. H., Madau, P., & Zycki, P. T. 1994, ApJ, 420, L57

Krolik, J. H., McKee, C. F., & Tarter, C. B. 1981, ApJ, 249, 422

Landi, E., & Phillips, K. J. H. 2006, ApJS, 166, 421

Laor, A. 1991, ApJ, 376, 90

Lightman, A. P., Lamb, D. Q., & Rybicki, G. B. 1981, ApJ, 248, 738

Lightman, A. P., & Rybicki, G. B. 1980, ApJ, 236, 928

Lightman, A. P., & White, T. R. 1988, ApJ, 335, 57

Magdziarz, P., & Zdziarski, A. A. 1995, MNRAS, 273, 837

Markowitz, A., et al. 2007, ApJ, 665, 209

Matt, G., Fabian, A. C., & Ross, R. R. 1993, MNRAS, 262, 179

—. 1996, MNRAS, 278, 1111

Matt, G., Perola, G. C., & Piro, L. 1991, A&A, 247, 25

Mendoza, C., Kallman, T. R., Bautista, M. A., & Palmeri, P. 2004, A&A, 414, 377

Mihalas, D. 1978, Stellar atmospheres (2nd ed.; San Francisco, CA: Freeman)

Nayakshin, S., & Kallman, T. R. 2001, ApJ, 546, 406

Nayakshin, S., Kazanas, D., & Kallman, T. R. 2000, ApJ, 537, 833

Page, K. L., O'Brien, P. T., Reeves, J. N., & Turner, M. J. L. 2004, MNRAS, 347, 316

Palmeri, P., Mendoza, C., Kallman, T. R., & Bautista, M. A. 2002, ApJ, 577, L119

—. 2003a, A&A, 403, 1175

Palmeri, P., Mendoza, C., Kallman, T. R., Bautista, M. A., & Meléndez, M. 2003b, A&A, 410, 359

Palmeri, P., Quinet, P., Mendoza, C., Bautista, M. A., García, J., & Kallman, T. R. 2008a, ApJS, 177, 408

Palmeri, P., Quinet, P., Mendoza, C., Bautista, M. A., García, J., Witthoeft, M. C., & Kallman, T. R. 2008b, ApJS, 179, 542

Poutanen, J., Nagendra, K. N., & Svensson, R. 1996, MNRAS, 283, 892

Pozdniakov, L. A., Sobol, I. M., & Sunyaev, R. A. 1979, A&A, 75, 214

Ralchenko, Y., Kramida, A. E., Reader, J., & NIST ADS Team. 2008, NIST Atomic Spectra Database, version 3.1.5 (Gaithersburg: NIST), http://physics.nist.gov/asd3

Reeves, J. N., et al. 2007, PASJ, 59, 301

Reis, R. C., Fabian, A. C., & Young, A. J. 2009, MNRAS, L297+

Ross, R. R., & Fabian, A. C. 1993, MNRAS, 261, 74

—. 2005, MNRAS, 358, 211

—. 2007, MNRAS, 381, 1697

Ross, R. R., Fabian, A. C., & Brandt, W. N. 1996, MNRAS, 278, 1082

Ross, R. R., Weaver, R., & McCray, R. 1978, ApJ, 219, 292

Rozanska, A., & Czerny, B. 1996, Acta Astron., 46, 233

Seaton, M. 1987, J. Phys. B: At. Mol. Opt. Phys., 20, 6363

Shakura, N. I., & Sunyaev, R. A. 1973, A&A, 24, 337

Summers, H. P. 2004, The ADAS User Manual, version 2.6, http://adas.phys.strath.ac.uk

Tanaka, Y., et al. 1995, Nature, 375, 659

Tarter, C. B., Tucker, W. H., & Salpeter, E. E. 1969, ApJ, 156, 943

Verner, D. A., & Yakovlev, D. G. 1995, A&AS, 109, 125

Watanabe, S., et al. 2003, ApJ, 597, L37

Witthoeft, M. C., Bautista, M. A., Mendoza, C., Kallman, T. R., Palmeri, P., & Quinet, P. 2009, ApJS, 182, 127

Yaqoob, T., et al. 2007, PASJ, 59, 283

Zycki, P. T., Krolik, J. H., Zdziarski, A. A., & Kallman, T. R. 1994, ApJ, 437, 597

This manuscript was prepared with the AAS LaTeX macros v5.2.